Intermittent sound generation and its control in a free-shear flow

André V. G. Cavalieri,[1,a)] Peter Jordan,[1,b)] Yves Gervais,[1,c)] Mingjun Wei,[2,d)] and Jonathan B. Freund[3,e)]

[1]*Département Fluides, Thermique, Combustion, Institut Pprime, CNRS-Université de Poitiers-ENSMA, UPR 3346, 43 Route de l'Aérodrome, Poitiers Cedex F86036, France*

[2]*Mechanical and Aerospace Engineering, New Mexico State University, P.O. Box 30001/Dept. 3450, Las Cruces, New Mexico 88003-8001, USA*

[3]*Mechanical Science & Engineering and Aerospace Engineering, University of Illinois at Urbana-Champaign, Urbana, Illinois 61801, USA*

(Received 24 June 2010; accepted 22 October 2010; published online 29 November 2010)

Comparisons are made between direct numerical simulations (DNS) of uncontrolled and optimally noise-controlled two-dimensional mixing layers in order to identify the physical mechanism responsible for the noise reduction. The analysis is carried out in the time domain to identify events that are significant in sound generation and which are acted upon by the control. Results show that a triple vortex interaction in the uncontrolled mixing layer radiates high-amplitude pressure waves to the far acoustic field; the elimination of this triple merging accounts for 70% of the noise reduction accomplished by a body force control applied normal to the shear layer. The effect of this control is shown to comprise vertical acceleration of vortical structures; the acceleration, whose action on the structures is convected across the control volume, leads to changes in their relative convection velocities and a consequent regularization of their evolution, which prevents the triple merger. Analysis of a longer time series for the DNS of the uncontrolled mixing layer using a wavelet transform identifies several similar intermittent, noisy events. The sound production mechanism associated with such noisy events can be understood in terms of cancellation disruption in a noncompact source region, such as described by a retarded-potential formalism. This shows that acoustic analogies formulated from the perspective of quadrupole acoustic sources are, in principle, useful for the modeling of such events. However, this study also illustrates the extent to which time-averaged statistical analysis of sound producing flows can mask the most important source activity, suggesting that intermittency should be explicitly modeled in sound prediction methodologies. © *2010 American Institute of Physics*. [doi:10.1063/1.3517297]

I. INTRODUCTION

Although research in aeroacoustics has made considerable progress since the pioneering work of Lighthill,[1] a clear mechanistic description of how free-shear flow turbulence generates sound remains elusive, and it is thus difficult to propose technical solutions that might reduce the sound power radiated by propulsive jets. In this context, direct numerical simulation (hereafter DNS) constitutes a valuable tool for studying the physics of the noise production. Although this kind of simulation is currently limited to flows with low Reynolds numbers, it facilitates a study of the fundamental vortex dynamics observed in turbulent flows; for a review of these and other applications, see Colonius *et al.*[2] and Wang *et al.*[3]

The work of Wei and Freund[4] provides a valuable opportunity for studying sound production mechanisms, and, in particular, for understanding what can be done to an unsteady vortical flow in order to make it significantly quieter. A two-dimensional, spatially evolving mixing layer was simulated, and by means of an adjoint-based formulation a series of optimally controlled flows were produced and compared with the uncontrolled baseline flow. Reductions in sound intensity of up to 6 dB in the far acoustic field were achieved; however, the differences between the controlled and uncontrolled flows were found to be subtle, with slight differences between the statistics of the various flows despite the one-order-of-magnitude reduction in radiated acoustic power. An analysis based on a proper orthogonal decomposition (POD), where these modes served a surrogates for Fourier modes in this streamwise inhomogeneous flow, showed that there was an underlying organization of the large structures due to the control, which was consistent with increased uniformity of their streamwise advection.

It is clear that such low Reynolds number, two-dimensional flow does not represent fully the turbulence dynamics of, for example, a three-dimensional high speed jet; hence, the extrapolation of the conclusions to other flows should be done with care. Nonetheless, in this simplified case important progress can be made with the understanding of the slight differences between a noisy, uncontrolled flow with quiet, controlled counterparts.

Some subsequent work addressed the differences be-

[a)]Electronic mail: andre.cavalieri@univ-poitiers.fr. Also at Instituto Tecnológico de Aeronáutica, Praça Marechal Eduardo Gomes, 50, Vila das Acácias, CEP 12228-900, São José dos Campos, Brazil.
[b)]Electronic mail: peter.jordan@univ-poitiers.fr.
[c)]Electronic mail: yves.gervais@univ-poitiers.fr.
[d)]Electronic mail: mjwei@nmsu.edu.
[e)]Electronic mail: jbfreund@illinois.edu.

tween the noisy and quiet mixing layers from other perspectives: Eschricht *et al.*[5] showed that there are differences in the wavenumber-frequency spectra of the hydrodynamic pressure fields of the uncontrolled and controlled flows, with less energy being found in the radiating sector of the controlled flow spectrum. In that same effort it was shown that two-point, two-time causality correlations between acoustic pressure and the Lighthill source term were affected by the control: the controlled flow showed more effective source cancellation and was thus a less efficient source of sound.

While these analyses provide a statistical perspective on the differences between the noisy and quiet mixing layers, the precise changes in the flow remained unclear. These approaches, being based on time-averaged statistics, masked the importance of local space-time events. They preclude the evaluation of intermittent events in the flow and the extent to which these may be important in the production of sound. Such intermittency has been found to be important in previous experimental and numerical jet noise studies. High levels of intermittency are also observed in the turbulence toward the end of the potential core in jets. Juvé *et al.*[6] used causality correlations in a Mach 0.9 jet to evaluate the instantaneous contribution of the source at the end of the potential core to the sound intensity at an angle of 30° to the downstream jet axis. The time traces of this contribution consisted of intermittent bursts interspersed by periods with near-zero values.

Hileman *et al.*[7] performed a similar study on an ideally expanded Mach 1.28 jet. The acoustic pressure at 30° had periods of relative quiet interspersed with large amplitude events. A continuous wavelet transform was used to estimate the frequency of the large amplitude peaks and the footprint of the relative quiet periods and of the high-pressure peaks could be detected in the resulting scalograms. The intense events in the acoustic field were used to select corresponding images from flow visualizations, and a subsequent POD analysis of these noise-producing events defined a characteristic loud flow signature, which corresponded to the intermittent intrusion of turbulent structures into the potential core.

The same techniques of Hileman *et al.*[7] were applied by Kastner *et al.*[8] to the Mach 0.9 jet DNS of Freund;[9] similar intermittent bursts were detected in the acoustic field, and the loud turbulent field was shown to have a truncated wave-packet structure, consistent with the conclusions of the experimental Mach 1.28 jet. Similar results have been reported by Bogey and Bailly[10] using a large eddy simulation of a Mach 0.9 jet. At the end of the potential core, intermittent vorticity bursts were observed, and these were correlated with positive pressure peaks in the far field at 40° from the downstream axis.

In this paper, we analyze data from the uncontrolled and controlled mixing layers of Wei and Freund[4] to identify loud intermittent events, particularly those that are suppressed by the control. In Sec. II we briefly describe the numerical simulations. Analysis of the acoustic field in Sec. III A shows that most of the acoustic energy for the uncontrolled flow is associated with a single event. In Secs. III B and III C we examine the vortex dynamics of both the controlled and uncontrolled flows and identify the essential difference between these. This specifically identified the loud flow event. A triple vortex merger leaves behind it an extended region of nearly irrotational flow; this local event momentarily disrupts the axial source cancellation mechanism and a strong pressure wave is emitted. In the controlled flow, the triple merger is prevented, and the source interference persists with much the same efficiency for the entire duration of the simulation.

We cannot of course claim that the triple vortex merger is the dominant mechanism of sound production in practical high-Reynolds-number free-shear flows; indeed it appears unlikely that even vortex pairing occurs or is important for noise generation in such flows, as discussed by Hussain and Zaman[11] and Bridges and Hussain.[12] On the other hand, the observation that the event constitutes an intermittent change in a basic vortex pattern, leading to a rupture of the space-time homogeneity of the hydrodynamic pressure signature and an associated high energy acoustic pressure burst, is a feature shared with the cited jet noise studies.[6–8,10] Furthermore, recent models (see Cavalieri *et al.*)[13,14] reproduce the intermittent behavior of coherent structures in a jet, and, based on an acoustic analogy with retarded-potential solutions, can lead to good predictions of the radiated sound by a turbulent jet.

In Sec. III D, the dynamics of the actuation is studied; we show that the action of the control involves a vertical displacement of vortical structures in the controlled flow, with which there is an associated change in their respective convection velocities and, consequently, their mutual interactions; the triple vortex merger is thus prevented. This indicates how actuation with a transverse force can regularize a given vortex pattern in order to suppress intermittency and thus reduce the radiated noise.

Finally, in Sec. IV, we use a continuous wavelet transform to analyze the acoustic pressure data taken from a longer time simulation of the uncontrolled mixing layer to objectively identify noisy events. Events of the same character as those identified by comparing the controlled and uncontrolled flows are found. These events share a noise signature, with time-scales in the wavelet domain between $60\delta_\omega/\Delta U$ and $200\delta_\omega/\Delta U$, and their behavior is intermittent, since four such events are identified in a time series of $6500\delta_\omega/\Delta U$ without observable periodicity.

II. THE TWO-DIMENSIONAL MIXING LAYER

The flow in this work is the same presented by Wei and Freund;[4] we will therefore only briefly describe it. A two-dimensional mixing layer was computed by direct numerical solution of the compressible, viscous flow equations. The Reynolds number was $\rho_\infty \Delta U \delta_\omega/\mu = 500$, with ρ_∞ as the ambient density of both uniform streams, ΔU as the velocity difference between the streams, δ_ω as the inflow vorticity thickness, and μ as the constant viscosity. The Mach numbers for the free streams were 0.9 and 0.2, and the Prandtl number was 0.7. The physical domain extended from $x=0$ to $x=100\delta_\omega$ and between $y=\pm 80\delta_\omega$.

The mixing layer was excited with eight frequencies f_i,

$$f_i = \frac{f_0}{4}(i + \alpha^{(i)}), \tag{1}$$

where f_0 is the estimated frequency for the most unstable mode according to linear stability theory, and $\alpha^{(i)}$ are random numbers between -0.5 and 0.5. To reduce the direct effect of the excitation in the radiated sound, the frequencies in Eq. (1) were excited with a solenoidal body force, which is relatively ineffective. This body force is applied upstream of the physical calculation domain. On account of this excitation, the mixing layer presents complex dynamics, without any observable periodicity. Although the Reynolds number is low, some aspects of noise generation by turbulence are expected to be represented.

The control, which was applied in a small square region covering $\delta_\omega < x < 7\delta_\omega$ and $-3\delta_\omega < y < 3\delta_\omega$ near the inflow, was modeled by a source term in the flow equations. Four different controls were applied: a mass source, x- and y-direction body forces, and an internal-energy source. These controls were chosen to be as general as possible: each space-time point of the discrete representation of the control forcing was treated as an independent control variable. We focused our analysis on the flow controlled by application of body forces in the y-direction, but the other controlled flows were also studied.

An optimal control algorithm was implemented. This involved an iterative process in which the adjoint of the perturbed and linearized flow equations was solved numerically to provide the sensitivity of the sound to changes in the control function $\phi(\mathbf{x},t)$. The objective functional to be minimized was

$$\mathcal{J}(\phi) = \int_{t_0}^{t_1} \int_{x_0}^{x_1} [p(\phi(\mathbf{x},t),\mathbf{x},t) - \bar{p}_o(\mathbf{x})]^2 \mathrm{d}\mathbf{x}\mathrm{d}t, \tag{2}$$

where p is the local pressure and $\bar{p}_o$ is the time-averaged local pressure for the uncontrolled flow. The spatial integration was performed in the region of uniform Mach 0.2 flow, along $y=-70\delta_\omega$, between $x_0=0$ and $x_1=100\delta_\omega$, and the temporal integration had as limits the start and end times of the control period.

Wei and Freund[4] showed that the controlled flows had noise reductions in the far field for all radiation angles; these reductions were up to 6 dB. The controlled mixing layers presented sound pressure spectra with reductions for the lower frequencies, which contained most of the sound energy; however, the controlled flows radiate more noise for the higher frequencies.

For a harmonically excited mixing layer, with excitation at frequencies f_0, $2f_0$, and six subharmonics of f_0, Wei and Freund[4] obtained results similar to those obtained by Colonius *et al.*,[15] with periodic vortex pairings at fixed locations. For this flow, Wei and Freund showed that their optimal control methodology does not produce any significant sound reduction. This suggests that the harmonically excited mixing layer, with its orderly structure, is near a lower limit for noise generation in a free-shear flow.

The control spectra were also analyzed in that paper and it was seen that the control was broadbanded, with significant energy content at frequencies other than the f_i excitation. The control spectrum also did not match the far field sound spectrum, indicating that the control worked via a nonlinear mechanism in the flow. Further details can be found in Wei[16] and Wei and Freund.[4]

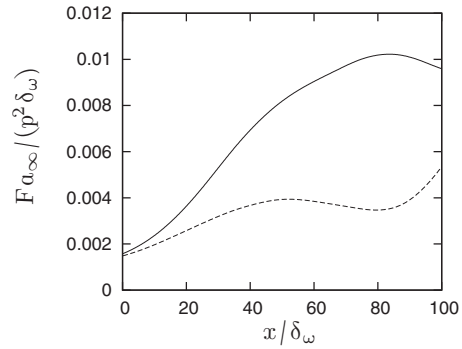

FIG. 1. Sound intensity at the target line for the (——) uncontrolled and (- - -) controlled mixing layers.

III. FLOW CHANGES BETWEEN THE UNCONTROLLED AND CONTROLLED FLOWS

A. Pressure data at the target line

Wei and Freund[4] found that despite the significant differences in the radiated noise between the uncontrolled and controlled flows, the changes in the flow are slight. In order to identify and understand the differences between the mixing layers, we first evaluate how the radiated pressure field is changed by control. Since the control objective is the noise reduction on a horizontal target line located at $y=-70\delta_\omega$ on the $M=0.2$ side of the mixing layer, we use this line to identify the space-time intervals where the sound reduction is most effective. We define

$$F(x) = \int_{t_0}^{t_1} [p(\phi(\mathbf{x},t),\mathbf{x},t) - \bar{p}_o(\mathbf{x})]^2 \mathrm{d}t \tag{3}$$

for both the uncontrolled and controlled flows. This allows a spatially localized assessment of the noise reduction; integration of $F(x)$ along the target line for a given control, ϕ, leads to the objective functional $\mathcal{J}$. Figure 1 shows $F(x)$ for the uncontrolled and y-direction body force controlled mixing layers. We see that although there is a noise reduction all along the target line, the control application is especially effective toward the downstream end of the flow domain.

Figure 2 shows pressure signals for three points on the target line: one upstream point, one centered, and one downstream. By means of these figures the temporal locality of the sound reduction can be assessed: a significant portion of the sound reduction at the downstream point occurs over a limited time interval.

Considering the point $(80\delta_\omega, -70\delta_\omega)$, we note that there is no noise reduction for the beginning of the simulation ($ta_\infty/\delta_\omega < 100$). As explained by Wei and Freund,[4] the noise at the target line is not controllable before a finite propagation period of the control effects. The most remarkable reduction in Fig. 2 happens between $ta_\infty/\delta_\omega = 300$ and $ta_\infty/\delta_\omega = 420$. In this interval the uncontrolled flow presents a large

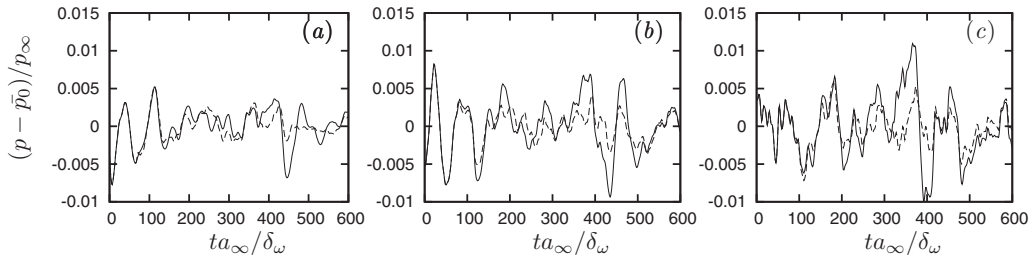

FIG. 2. Pressure for the (——) uncontrolled and (- - - -) controlled mixing layers in the points (a) $x/\delta_\omega=20$, (b) $x/\delta_\omega=50$, and (c) $x/\delta_\omega=80$ of the target line.

positive pressure peak, followed by a negative peak of similar level; the controlled flow presents much smaller amplitude pressure waves during the same period. We thus see that most of the sound reduction is achieved by eliminating this one large peak. In fact, 70% of the reduction of the function F at this point happens during the period $300<ta_\infty/\delta_\omega<420$. This suggests that the noise reduction is due to the elimination of a single event in the flow.

B. Flow dynamics for the uncontrolled and controlled flows

Figure 3 shows visualizations of the pressure and vorticity fields for the uncontrolled mixing layer at six different times, and in Fig. 4 visualizations for the controlled case are shown at the same times. The time $ta_\infty/\delta_\omega=367.9$ [Figs. 3(d) and 4(d)] corresponds to the arrival of the large positive pressure peak at the point $(80\delta_\omega,-70\delta_\omega)$ for the uncontrolled mixing layer, as shown in Fig. 2. In Fig. 3(d) this can be seen as a group of positive contours. For the controlled mixing layer, we also see positive contours in Fig. 4(d) around the point $(80\delta_\omega,-70\delta_\omega)$, but with a much smaller amplitude.

The time $ta_\infty/\delta_\omega=312.5$ [Figs. 3(a) and 4(a)] was chosen by calculating the propagation time of a wave in a uniform flow at $M=0.2$ between the points $(80\delta_\omega,-20\delta_\omega)$ and $(80\delta_\omega,-70\delta_\omega)$. For the uncontrolled mixing layer, we can see in Fig. 3(a) that there is high-pressure around the point $(80\delta_\omega,-20\delta_\omega)$, close to the zero-vorticity region lying between the pair of vortices at $x=60\delta_\omega$ and a zone of vorticity that has just crossed the downstream boundary of the computational domain. By following in succession Figs. 3(b) and 3(c) we see how this high-pressure propagates to the $(80\delta_\omega,-70\delta_\omega)$ point on the target line. We see also that there is propagation of a similar high-pressure wave to the $M=0.9$ side of the mixing layer. A similar propagation occurs in the controlled mixing layer, but with a much smaller amplitude, as seen in Figs. 4(a)–4(d). The clearest difference in the vortex dynamics between this flow and the uncontrolled mixing layer is the presence of a vortical region near $x=90\delta_\omega$ for the controlled mixing layer at $ta_\infty/\delta_\omega=312.5$. This last vortex is not visible in Fig. 3(a).

The negative pressure peak for the uncontrolled mixing layer at the point $(80\delta_\omega,-70\delta_\omega)$, shown in Fig. 2, corresponds to the time $ta_\infty/\delta_\omega=396.5$ shown in Fig. 3(f). As was done for the positive pressure wave, we calculate the propagation time of this wave to estimate its origin, and the resulting time is $ta_\infty/\delta_\omega=341.0$, shown in Fig. 3(b). We can see in the uncontrolled mixing layer that a vortical structure enters the long quasi-irrotational, high-pressure region of flow. As

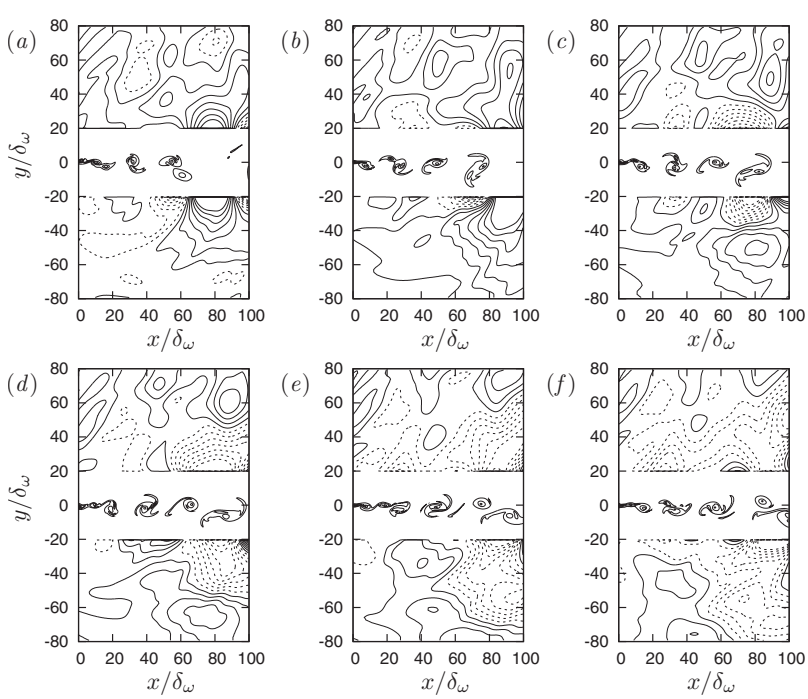

FIG. 3. Uncontrolled mixing layer at times ta_∞/δ_ω =(a) 312.5, (b) 341.0, (c) 354.5, (d) 367.9, (e) 383.0, and (f) 396.5. Center: vorticity modulus, contours from 0.07 to $1.4\Delta U/\delta_\omega$. Outer regions: pressure, contours from -0.02 to $0.02p_\infty$. Negative contours are dashed.

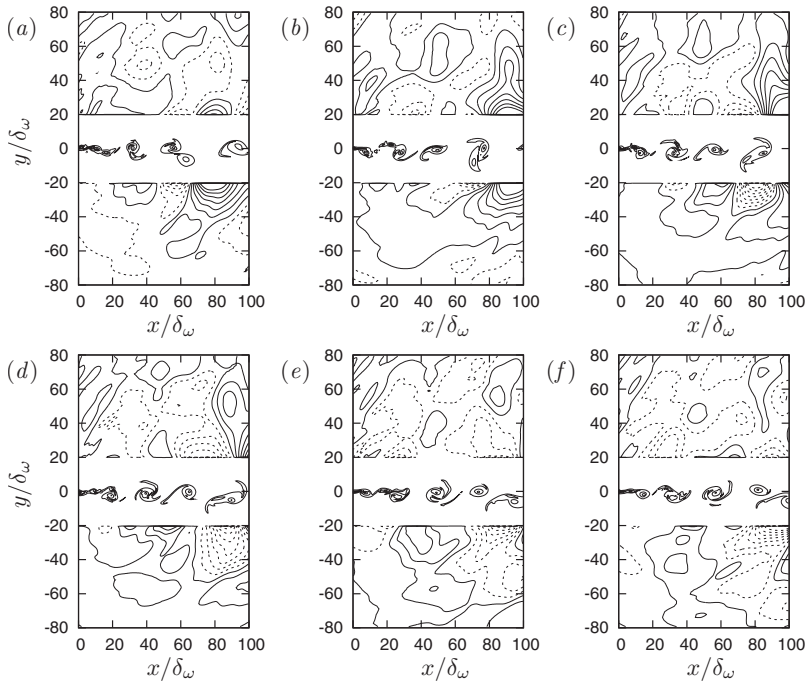

FIG. 4. Controlled mixing layer. Center: vorticity modulus. Outer regions: pressure. Same contours and times of Fig. 3.

this vortex is convected to the end of the computational domain [Figs. 3(c)–3(f)], we see the formation of a low-pressure wave, which propagates to the far field and arrives at $(80\delta_\omega, -70\delta_\omega)$ with a high amplitude. The same times for the controlled mixing layer [Figs. 4(c)–4(f)] show the propagation of a negative pressure wave to $(80\delta_\omega, -70\delta_\omega)$, but with reduced amplitude.

Although the vorticity contours of the mixing layers at $ta_\infty/\delta_\omega = 341.0$ (the time where the low pressure wave originates) are similar, for the uncontrolled flow we see a pocket of vorticity enter an extended region of nearly irrotational flow; for the controlled mixing layer, the passage of a similar concentration of vorticity occurs, but the distances between successive vortical regions are more uniform. If we consider the generation of sound-waves from a free-shear flow to be the result of incomplete interference between regions of positive and negative stress, or pressure, as retarded-potential type solutions for the radiated pressure would have us believe, then we see that the occurrence of an intermittent event can significantly disrupt the interference. During this period, the mutual cancellations, which occur between neighboring vortices, are unbalanced, making possible the generation of a large amplitude sound wave. This assertion is consistent with the conclusions drawn by Wei and Freund[4] and Eschricht *et al.*,[5] but we have here identified the actual flow event driving it and so we are in a position to propose a local explanation for the sound production mechanism and its control, free from the cloudiness of averaging.

C. Intermittency in the uncontrolled mixing layer

The difference in the evolution of the vorticity of the uncontrolled and controlled mixing layers is due to a triple vortex interaction that occurs in the uncontrolled flow. Figure 5(a) shows the temporal evolution of this event up to $ta_\infty/\delta_\omega = 312.5$, which is shown in Fig. 3(a). We see that this triple merger, which happens only once in the simulation of the uncontrolled mixing layer, leads to the extended irrotational region in Fig. 3(a). A large vortical structure is created by this interaction. The two smaller vortices rotate at high speed around the larger structure, causing the agglomeration to enter the downstream absorbing buffer zone earlier than their controlled counterparts, shown in Fig. 5(b). The controller modifies the flow dynamics such that the triple merger is eliminated. This reduces the extent and level of the high-pressure irrotational region and, as we have seen, the amplitude of the propagated sound wave.

In order to verify that the occurrence of this extended high-pressure region is indeed an intermittent event, we show, in Fig. 6, visualizations of the vorticity field for all other times where a vortex is observed at $x = 60\delta_\omega$. We see

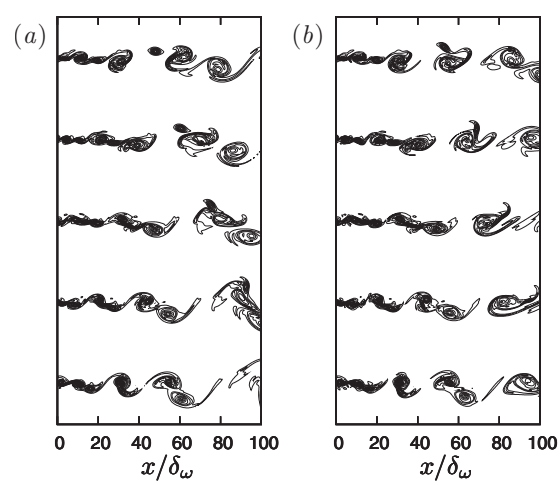

FIG. 5. Instantaneous vorticity modulus for the (a) uncontrolled and (b) controlled mixing layers at times $ta_\infty/\delta_\omega = 245.3$, 262.1, 278.9, 295.7, and 312.5, from top to bottom. Contours range from $0.014\Delta U/\delta_\omega$ to $0.7\Delta U/\delta_\omega$.

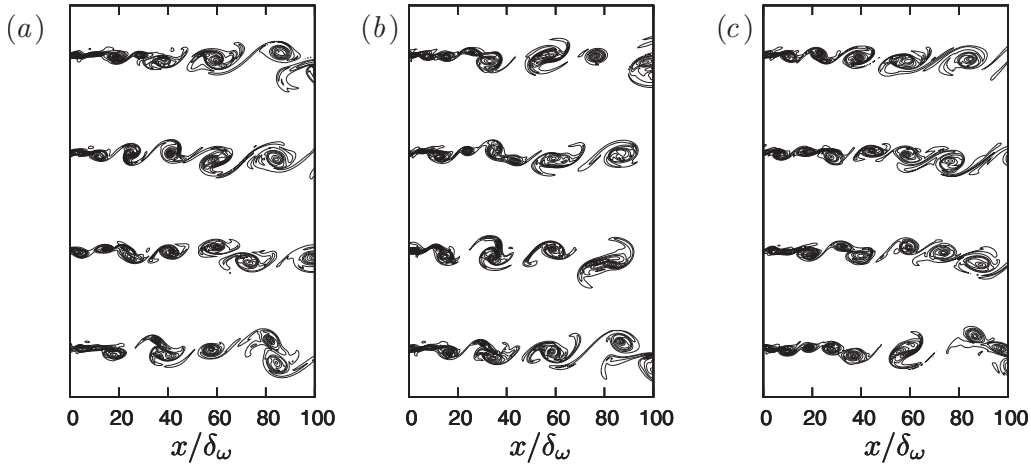

FIG. 6. Instantaneous vorticity for the uncontrolled mixing layer at times ta_∞/δ_ω=(a) 13.4, 58.8, 87.4, and 117.6; (b) 151.2, 206.6, 357.8, and 399.8; and (c) 445.2, 482.2, 505.7, and 544.3. Contour levels range from $0.014\Delta U/\delta_\omega$ to $0.7\Delta U/\delta_\omega$.

that for each image there is at least one other vortex in the domain between $x=60\delta_\omega$ and $x=100\delta_\omega$; there is never an irrotational region as long as that shown in Fig. 3(a). Again, these mechanistic interpretations are consistent with the conclusions drawn by Wei and Freund,[4] who showed, by means of a POD analysis, that the controlled flow approaches a pure advective behavior. The first POD eigenfunctions of the controlled flows are coupled in pairs of similar energy and their representation in the phase plane has circular traces. These are characteristics of flows with pure convection of structures, with a form such as $\cos(\omega t-kx)$, whose POD representation is $\cos\omega t\cos kx+\sin\omega t\sin kx$, with consequent circles in the phase plane. This is not the case for the uncontrolled flow. We see here that the elimination of the vortex merger constitutes a change that is synonymous with a harmonization of the mixing layer, which approaches, for the controlled flow, the intrinsically quiet pattern of pure subsonic advection. In the controlled mixing layer, the vortex pattern becomes more uniform as the triple merging is changed into vortex dynamics that are closer to what happens in the other times of the simulation. We see that the downstream part of the controlled mixing layer shown in Fig. 4(a) is much closer to the vortex configurations of Fig. 6 than the uncontrolled mixing layer at the same time, shown in Fig. 3(a).

This change in the vortex pattern at the end of the mixing layer can also be seen by evaluation of

$$\xi(x,t)=\int_{-\infty}^{\infty}\omega(x,y,t)\mathrm{d}y, \tag{4}$$

which is the radially integrated instantaneous vorticity at x. This integrated vorticity is shown in Fig. 7 for two positions of the mixing layer.

In Fig. 7(b) we see that the temporal pattern of integrated vorticity at $x/\delta_\omega=80$, representing the downstream end of the mixing layer, becomes more regular for the controlled flow. The strengths of the vortices are more homogeneous, as is the temporal spacing between the vorticity peaks. This is particularly the case between $ta_\infty/\delta_\omega=200$ and $ta_\infty/\delta_\omega=350$, which corresponds to the interval over which the triple interaction takes place. On the other hand Fig. 7(a) shows that only slight changes are observed at $x/\delta_\omega=20$. The control is thus effected via small changes in the flow in the upstream region, becoming more noticeable as the vortices are convected and interact. The pairing processes are modified by the action of control and these approach the behavior observed for a mixing layer with harmonic excitation, which is an intrinsically quiet flow.

So far we have only shown results for the y-direction body force actuation. But similar results are observed for the other types of control implemented by Wei and Freund.[4] In all cases the triple vortex interaction is eliminated, and with it the extended region of high-pressure. Figure 8 shows, for

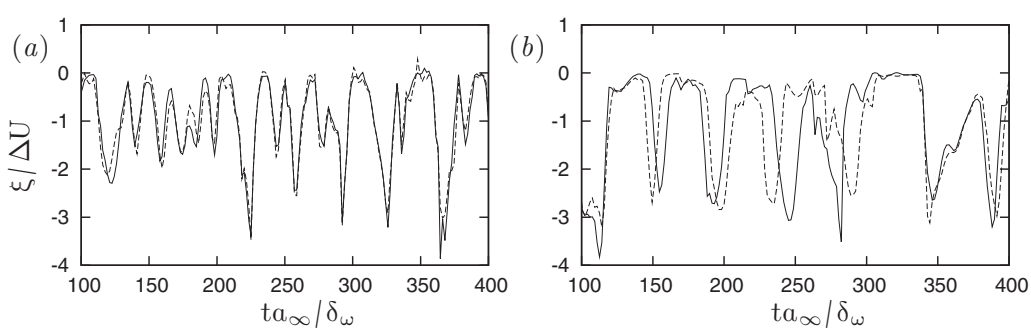

FIG. 7. Integrated vorticity at (a) $x/\delta_\omega=20$ and (b) $x/\delta_\omega=80$: (——) uncontrolled and (- - - -) controlled flow.

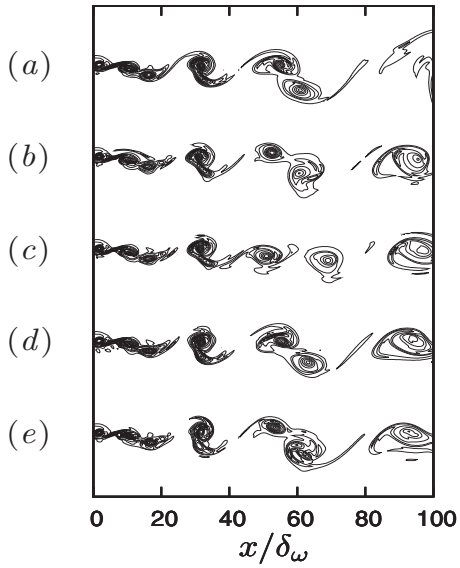

FIG. 8. Vorticity contours at $ta_\infty/\delta_\omega=312.5$ for the flows with (a) no control, (b) mass source control, (c) x-direction body force control, (d) y-direction body-force control, and (e) internal-energy source control. Same contours of Fig. 6.

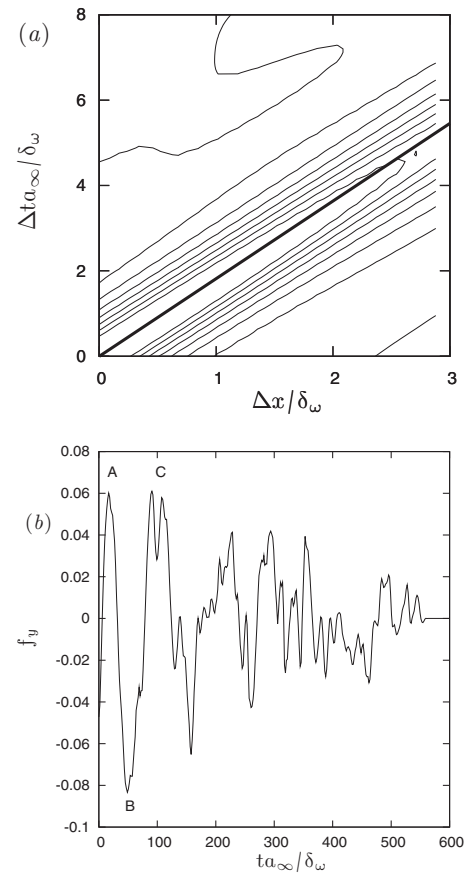

FIG. 9. (a) Space-time correlation at $y=0$ for the optimal y-direction body force control; thin lines show normalized correlation levels from 0.1 to 0.8, and the thick line corresponds to the convection Mach number 0.55. (b) Integrated y-direction body force control.

each of the control cases, the vorticity field at $ta_\infty/\delta_\omega=312.5$, which corresponds to the long high-pressure region for the uncontrolled mixing layer [Fig. 8(a)]. Although there are slight differences between the vortex patterns, all of them present a smaller zero-vorticity region than the one shown for the uncontrolled flow in Fig. 3(a). The extent of this region is much closer to that shown in Fig. 6. Thus, all of the control formulations prevent the formation of the extended high-pressure zone, which is the essential difference between the controlled and uncontrolled flows.

D. Optimal control dynamics for the *y*-direction body force

Having identified the change in the mixing layer responsible for the noise reduction, we now want to understand the control mechanism, by which the suppression of the triple vortex pairing was achieved. This is of practical interest, as it can suggest how a physical actuator might be conceived for, say, the initial mixing layer of a jet.

We can readily see that the y-direction body force control "follows" the vortical structures in so far as the forces are correlated according to the convection speed, as seen in Fig. 9(a). This characteristic, which was also identified by Wei,[16] is an indication that the control acts on the vortices in a coherent manner as they advect through the control region $\mathcal{C}$.

To estimate the net effect of the control ϕ with distributed y-direction body forces per unit volume, which in the y-momentum equation corresponds to

$$\frac{D(\rho v)}{Dt}=-\frac{\partial p}{\partial y}+\phi-\frac{1}{\mathrm{Re}}\left(\frac{4}{3}\frac{\partial^2 v}{\partial y^2}+\frac{\partial^2 v}{\partial x^2}+\frac{1}{3}\frac{\partial^2 u}{\partial x\,\partial y}\right), \tag{5}$$

we integrate it over the control region $\mathcal{C}$,

$$f_y(t)=\int\int_{\mathcal{C}}\phi(\mathbf{x},t)\mathrm{d}\mathbf{x}. \tag{6}$$

Figure 9(b) shows the net y-direction force during the simulation of the controlled mixing layer. We label the distinct peaks of the total force toward the beginning of simulations A, B, and C for later reference.

We see in Fig. 10 the vortical structures that pass through the $\mathcal{C}$ region at times corresponding to the peaks indicated in Fig. 9(b), as well as a representation of the applied control. The vortices are labeled according to the corresponding peaks in Fig. 9(b); since there are two C peaks, two C vortical structures are shown. Each peak in the net force corresponds to a relatively uniform distribution of ϕ over the control region, either in the positive (A and first C peak) or in the negative (B) y-direction. On the other hand, for the second C vortex in Fig. 10(d) we see that the force field is less uniform than those applied to the other structures [Figs. 10(a)–10(c)]; however, even in that case most of the distributed force acts in the same direction, and, as will be shown later, the observed global control effect for the second C vortex is similar to that identified for the other structures.

We can therefore interpret the y-direction body force control for the marked peaks as an approximately uniform

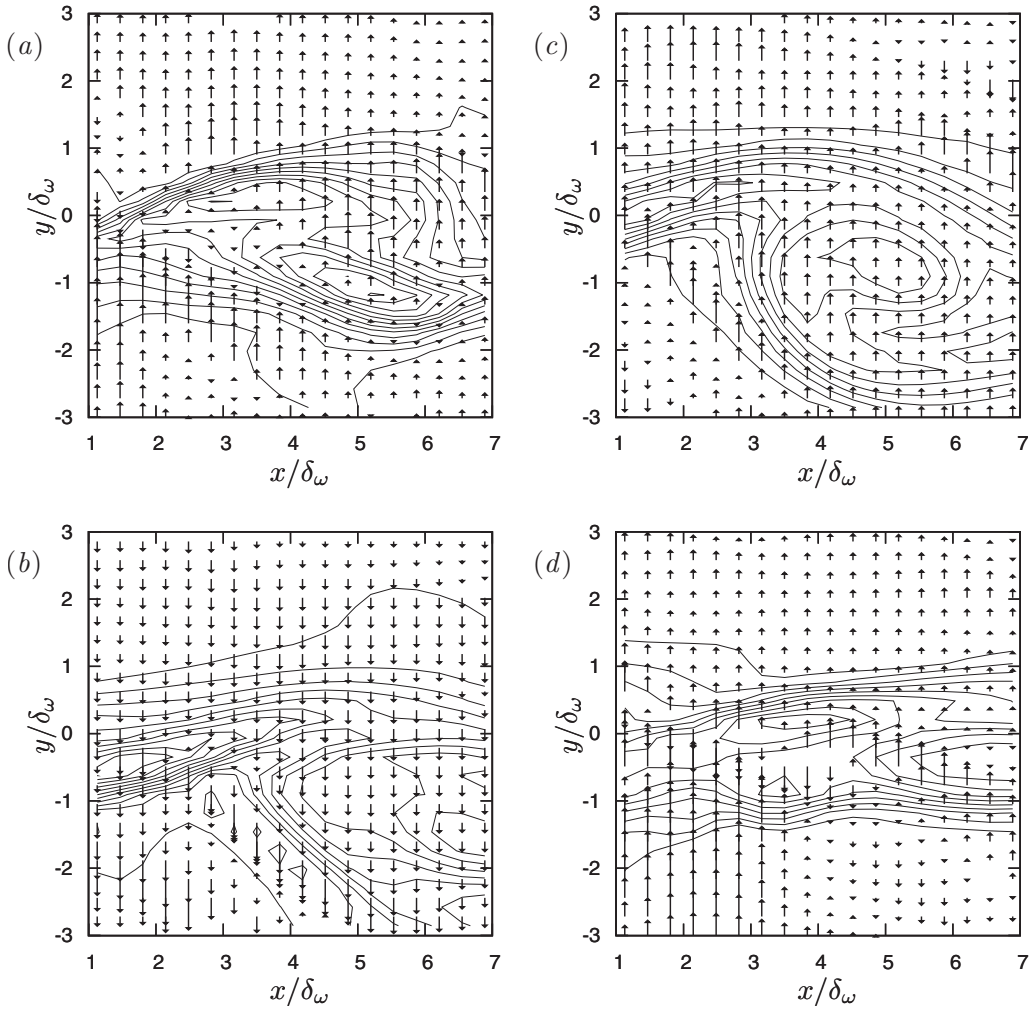

FIG. 10. Vorticity contours at the control region $\mathcal{C}$, and applied control (arrows), at (a), $ta_\infty/\delta_\omega=16.8$ (A vortex); (b), $ta_\infty/\delta_\omega=47.0$ (B vortex); (c), $ta_\infty/\delta_\omega=90.7$ and (d), $ta_\infty/\delta_\omega=107.5$ (C vortices).

force distribution that follows the convection of the vortices through the control region. The effect is a predominantly vertical acceleration of the structures, without any significant changes in the vorticity.

We confirm this conclusion with the observation of Fig. 11, where we follow the convection of the A vortex in the uncontrolled and controlled mixing layers. The effect of the positive forces applied to the A vortex [Fig. 10(a)] can be seen in its downstream evolution. For the controlled flow, there is a positive vertical displacement of the vortex in the controlled flow [Figs. 11(f)–11(h)] compared to the uncontrolled mixing layer [Figs. 11(b)–11(d)]; this is especially visible in Fig. 11(h). Although the body force is only applied upstream, the continued displacement of the vortex is pre-

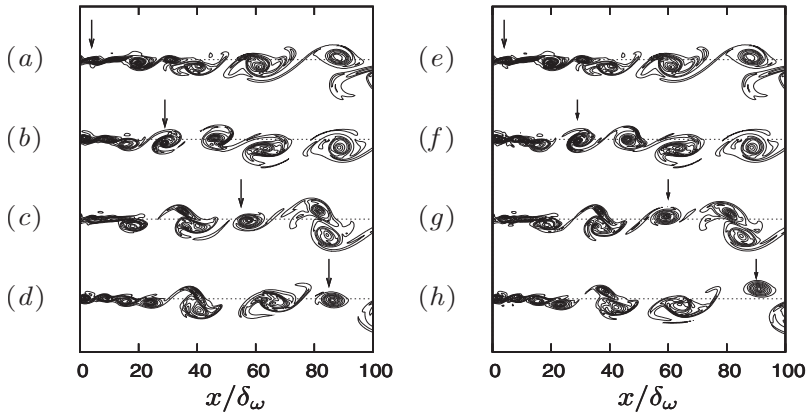

FIG. 11. Vorticity contours for: (a) and (e), $ta_\infty/\delta_\omega=16.8$; (b) and (f), $ta_\infty/\delta_\omega=67.2$; (c) and (g), $ta_\infty/\delta_\omega=117.6$; and (d) and (h), $ta_\infty/\delta_\omega=168.0$. Contours (a)–(d) refer to the uncontrolled mixing layer and (e)–(h) to the y-direction body force control. Arrows follow the convection of the A vortex. Same contours of Fig. 6.

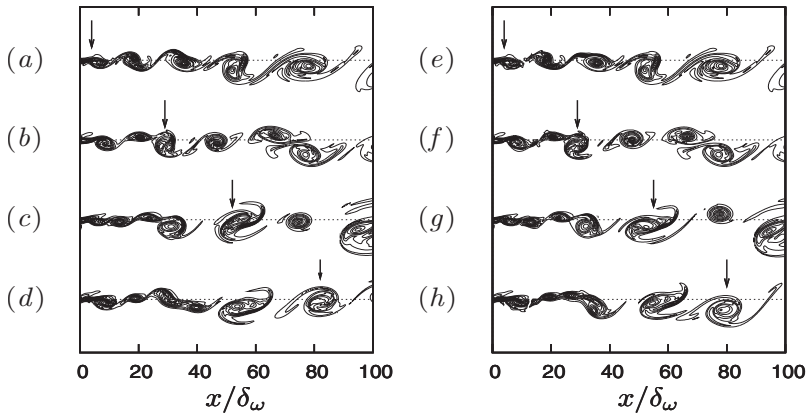

FIG. 12. Vorticity contours for: (a) and (e), $ta_\infty/\delta_\omega=47.0$; (b) and (f), $ta_\infty/\delta_\omega=97.4$; (c) and (g), $ta_\infty/\delta_\omega=147.8$; and (d) and (h), $ta_\infty/\delta_\omega=198.2$. Contours (a)–(d) refer to the uncontrolled mixing layer and (e)–(h) to the y-direction body force control. Arrows follow the convection of the B vortex. Same contours of Fig. 6.

sumably due to the intrinsic instability of the mixing layer: a small disturbance in the position of an upstream structure can be amplified downstream by its interaction with the neighboring vortices.

Furthermore, since the Mach numbers of the upper and lower streams are, respectively, 0.9 and 0.2, an upward displacement of a structure leads to a higher convection velocity. This effect is also observed in Fig. 11, where the displaced vortex in the controlled mixing layer arrives earlier at the downstream end of the physical domain.

Having understood how a vertical force changes the dynamics of the A vortex, we can proceed to evaluate how the control suppresses the triple vortex merger. This is done by the B and C peaks in the y-direction body force, shown in Fig. 9(b).

Figure 12 shows the evolution of the B vortex. Since the B feature in Fig. 9(b) is negative, we see for the controlled mixing layer [Figs. 12(e)–12(h)] a negative vertical displacement of the B vortex, compared to the uncontrolled flow [Figs. 12(a)–12(d)]. As the B vortex comes into the lower stream, its convection speed decreases.

The action of the C peaks in the body force can be followed in Fig. 13. The C peaks in Fig. 9(b) are applied when two close vortices pass in the control region $\mathcal{C}$. These two vortices are marked with full arrows in Figs. 13(a) and 13(d) for the uncontrolled and controlled flows, respectively. The B vortex is also marked in Fig. 13 with dashed arrows. The two C vortices pair just after leaving the $\mathcal{C}$ region. This C structure is directed upward, as a consequence of the positive forces applied in the controlled mixing layer; so, its convection speed is increased.

A clear distinction can then be made between the uncontrolled and controlled flows: in the controlled mixing layer, the faster C vortex approaches the slower B vortex, initiating a pairing process [Fig. 13(g)]; on the other hand, the C vortex in the uncontrolled mixing layer interacts with the upstream vortical structures, leading to the triple vortex interaction analyzed in Sec. III C [Figs. 13(c) and 13(d)]; note that the last time in Fig. 13, $ta_\infty/\delta_\omega=258.7$, shows the beginning of the triple pairing process seen in Fig. 5(a). We thus have two vortex pairings for the controlled mixing layer, instead of the acoustically efficient vortex-tripling.

To summarize, the main effect of the y-direction body force control can be understood as a series of displacements of the vortical structures, with subsequent changes in their convection velocities that lead to a more regular pattern. This conclusion is of practical interest for aeroacoustic noise control: bursts of acoustic energy may be suppressed by an actuation capable of eliminating the intermittent dynamics of flows, and for a sheared flow, such as the initial mixing layer of a jet, this can be accomplished with an appropriate transverse force.

Similar studies of the other controlled mixing layers reveal that the vortex dynamics in all the controlled cases are similar to what is observed for the y-direction body force control. Indeed, we see in Fig. 14 that for all the cases the A

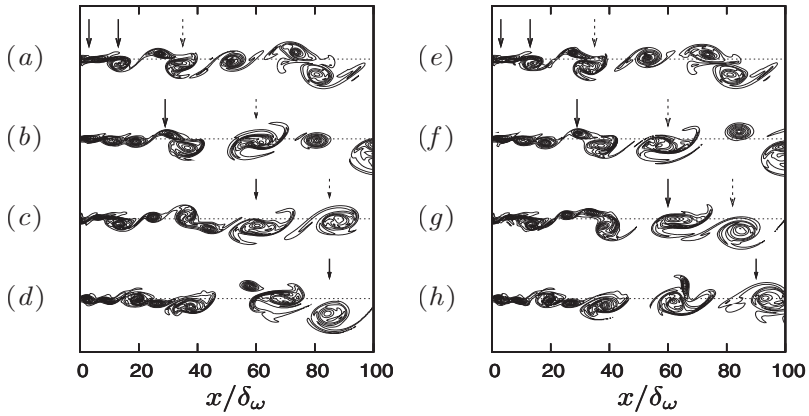

FIG. 13. Vorticity contours for: (a) and (e), $ta_\infty/\delta_\omega=107.5$; (b) and (f), $ta_\infty/\delta_\omega=157.9$; (c) and (g), $ta_\infty/\delta_\omega=208.3$; and (d) and (h), $ta_\infty/\delta_\omega=258.7$. Contours (a)–(d) refer to the uncontrolled mixing layer and (e)–(h) to the y-direction body force control. Full arrows follow the convection of the C vortices and dashed arrows follow the B vortex. Same contours of Fig. 6.

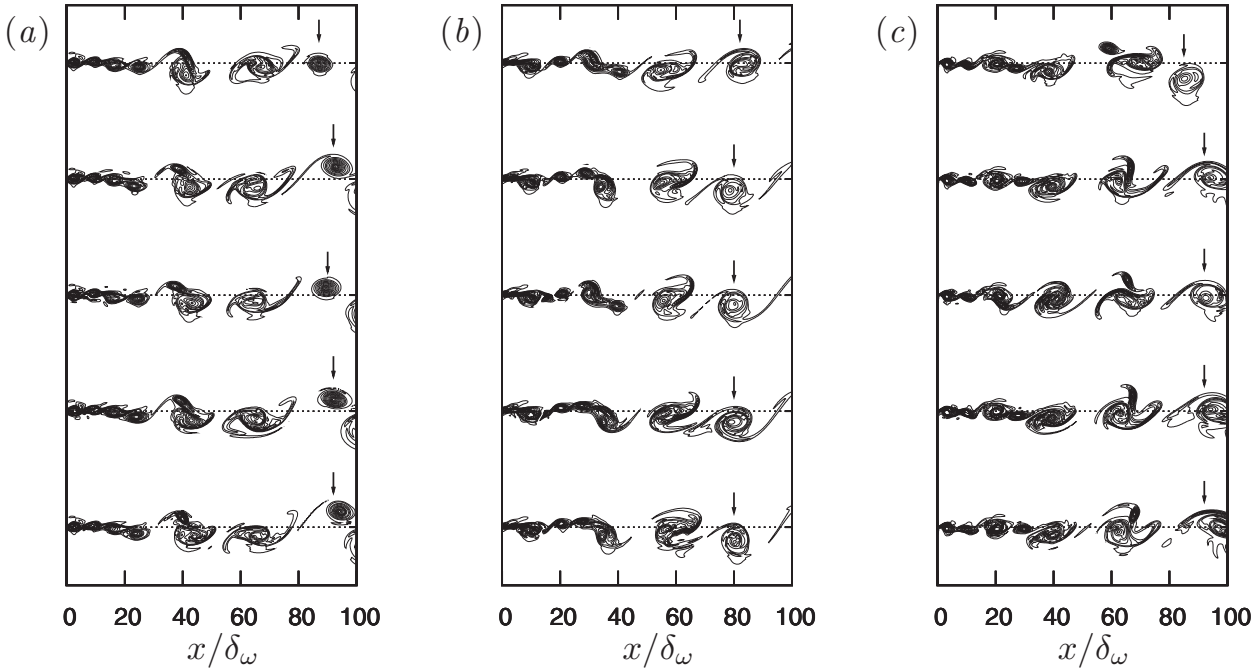

FIG. 14. Vorticity contours for: (a) $ta_\infty/\delta_\omega=168.0$, with the A vortex highlighted, (b) $ta_\infty/\delta_\omega=198.2$, with the B vortex highlighted, and (c) $ta_\infty/\delta_\omega=258.7$, with the C vortex highlighted. Contours from the top downward refer, respectively, to the uncontrolled mixing layer, the mass source control, the x- and the y-direction body force controls, and the internal-energy control. Same contours of Fig. 6.

vortex is displaced upward, the B vortex downward, and the C vortices upward. These vertical displacements likewise lead to higher or lower convection speeds depending on the side of the mixing layer into which the structures are displaced. However, the y-momentum control is the most intuitive; the dynamics of the other controls defies such a simple mechanistic explanation.

IV. DETECTION OF INTERMITTENT RADIATION

To make the analysis more quantitative, we analyzed the pressure signal at the same point $(80\delta_\omega,-70\delta_\omega)$ by means of a continuous wavelet transform. The pseudospectra computed this way are localized in both time and time-scale.

Farge[17] provides a complete review of these methods. The continuous wavelet transform is

$$\tilde{p}(s,t)=\int_{-\infty}^{\infty}p(\tau)\psi(s,t-\tau)\mathrm{d}\tau, \tag{7}$$

where s is the time-scale of the wavelet function. We used Paul's wavelet, defined for $s=1$ with an order m as

$$\psi(1,t)=\frac{2^m i^m m!}{\sqrt{\pi(2m)!}}[1-i(t)]^{-(m+1)}. \tag{8}$$

This is a complex-valued wavelet function; for $m=4$ its real and imaginary parts are shown in Fig. 15. The choice of this wavelet function with $m=4$ is due in particular to its imaginary part, which approximates the shape of the noisy signature of the uncontrolled mixing layer seen in Fig. 2(c), but with a negative sign. We thus expect that similar signatures will have a continuous wavelet transform with high energy content in a small scale range and in a reduced interval of the simulation. The other scales are obtained by dilatation of the so-called mother wavelet, with a normalization by $\sqrt{s}$ in order to maintain unit energy,

$$\psi(s,t-\tau)=\frac{1}{\sqrt{s}}\psi\left(1,\frac{t-\tau}{s}\right). \tag{9}$$

A longer DNS simulation of the uncontrolled flow was used (ten times that of Wei and Freund).[4] The same code was used for the simulation, with an identical grid and the same simulation parameters. The results are obviously identical over the time interval considered in that paper.

The continuous wavelet transform was applied to the pressure signal at the point $(80\delta_\omega,-70\delta_\omega)$ of this long simulation, the same point used in the analysis in Sec. III A [see Fig. 2(c)]. The resulting scalogram is shown in Fig. 16. In Fig. 16(a), which corresponds to the original simulation up to $ta_\infty/\delta_\omega=626.6$, there is a clear peak identified at $ta_\infty/\delta_\omega \simeq 380$, which corresponds to that analyzed in Sec. III A. The data are continued to longer times in Fig. 16(b). Here, we see

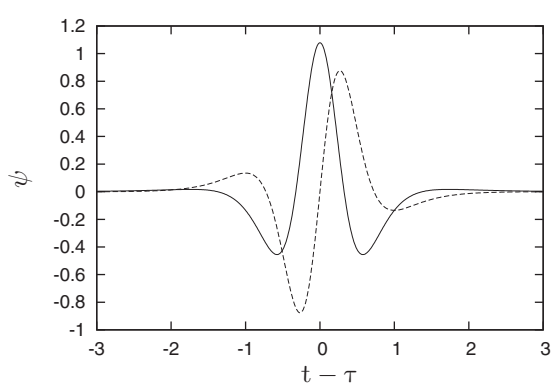

FIG. 15. Paul's wavelet: (——) real and (- - - -) imaginary parts.

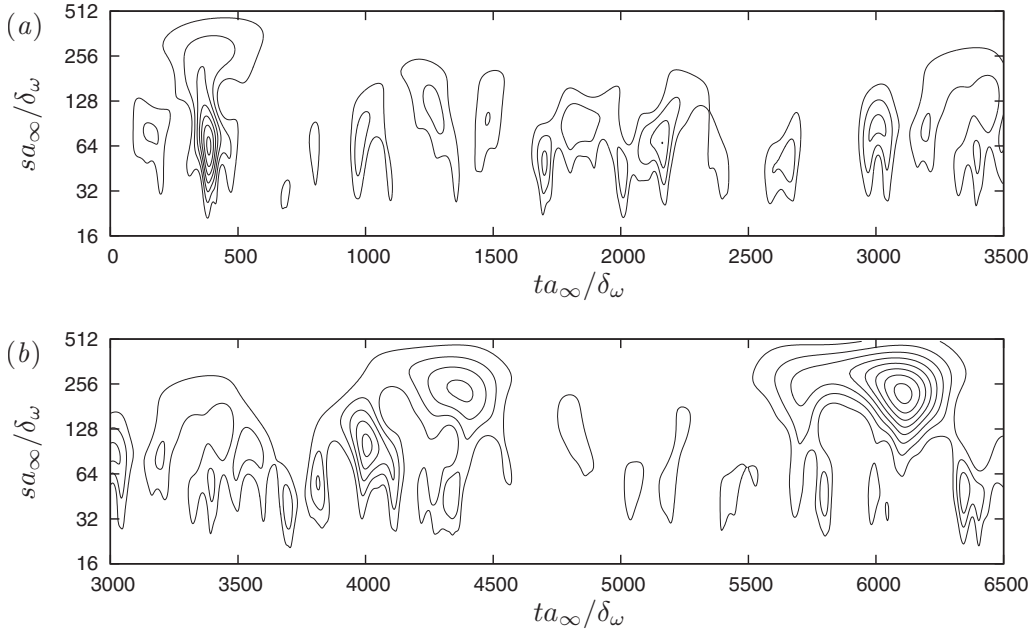

FIG. 16. Wavelet spectrum for the (a) first and (b) second parts of the simulation. Levels are uniformly distributed between 0 and $0.03(p_\infty\delta_\omega/a_\infty)^2$ in steps of $0.003\ (p_\infty\delta_\omega/a_\infty)^2$.

that in the continued longer simulation there are similar peaks concentrated around $ta_\infty/\delta_\omega \simeq 4000$, $ta_\infty/\delta_\omega \simeq 4400$, and $ta_\infty/\delta_\omega \simeq 6100$. We note that the results of Fig. 16 are similar to the experimental wavelet spectrum shown by Hileman *et al.*,[7] which showed periods of relative quiet interspersed with noise generation events.

To isolate the events that correspond to the peaks in the scalogram, we performed a filtering operation based on a threshold α,

$$\tilde{p}_f(s,t) = \begin{cases} \tilde{p}(s,t) & \text{if } |\tilde{p}(s,t)|^2 > \alpha \\ 0 & \text{if } |\tilde{p}(s,t)|^2 < \alpha. \end{cases} \tag{10}$$

The filtered pressure in the wavelet basis is then transformed back to the time domain by means of an inverse continuous wavelet transform. For the inverse transform we used the expression presented by Farge,[17] which gives

$$p_f(t) = \frac{1}{C_\delta}\int_{0^+}^{\infty} \frac{\tilde{p}_f(s,t)}{s^{3/2}}\mathrm{d}s, \tag{11}$$

where C_δ is obtained by the Fourier transform of the mother wavelet $\hat{\psi}(1,\omega)$,

$$C_\delta = \frac{1}{\sqrt{2\pi}}\int_{0^+}^{\infty} \frac{\hat{\psi}(1,\omega)}{\omega}\mathrm{d}\omega. \tag{12}$$

The numerical application of the continuous wavelet transform was performed for a total of 120 time-scales, defined as

$$s_j = 2^{[(j-1)\Delta s]}s_0, \tag{13}$$

where s_0 is the first scale. We chose s_0 to be twice the data-writing period in the simulation and Δs as $s_0/100$. The scale distribution of Eq. (13) allowed us to use the numerical formulation of Torrence and Compo.[18] Application with $\alpha=0$ recovered the original time series with a relative error of 2.2% with the chosen set of scales.

We chose as a filter $\alpha=0.009(p_\infty\delta_\omega/a_\infty)^2$, since above this value only the high energy concentrations shown in Fig. 16, analogous to that found at the beginning of the simulation, are thus retained. The results of this filtering operation applied to the beginning of the simulation are presented in Fig. 17. We see that the filtered pressure is zero in all but a reduced interval, where the vortex merger signature analyzed in Sec. III A is captured. For the remainder of the simulation, the reconstructed pressure signal is mostly zero, but at the intervals where there are energy concentrations in both time and time-scale we see clear peaks for the pressure. We see in Fig. 18(a) that the filtered pressure around $ta_\infty/\delta_\omega=4000$ has a pattern similar to that observed in Fig. 17, and which was related to the triple vortex interaction in Sec. III C. In Figs. 18(b)–18(e) we see vorticity contours at the center of the mixing layer at times prior to the arrival of the mentioned

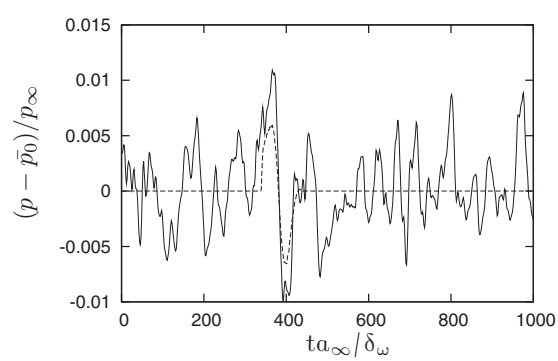

FIG. 17. Wavelet filtering at $(80\delta_\omega, -70\delta_\omega)$: (——) original and (- - -) filtered pressures.

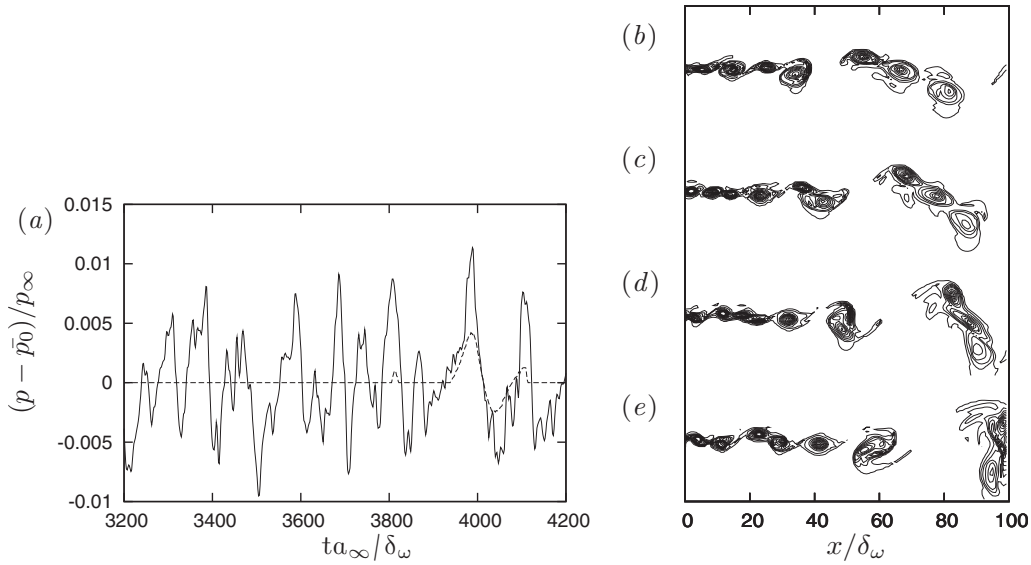

FIG. 18. (a) Wavelet filtering, (——) original and (- - -) filtered pressures. [(b)–(e)] Vorticity contours at ta_∞/δ_ω=3899.3, ta_∞/δ_ω=3916.1, ta_∞/δ_ω=3932.9, and ta_∞/δ_ω=3949.7. Contours range from $0.014\Delta U/\delta_\omega$ to $0.7\Delta U/\delta_\omega$.

pressure peaks. There is a triple vortex merger similar to that shown in Fig. 5(a).

Figures 19 and 20 show results for the other intervals of the simulation, when there are nonzero values for the filtered pressure. We see again in Figs. 19(a) and 20(a) a similar pressure signature as that of Figs. 17 and 18(a); and the corresponding vorticity contours, shown in Figs. 19(b)–19(e) and 20(b)–20(e), show triple vortex mergers to occur in each case, just prior to the arrival of the high-amplitude pressure wave at the considered point.

Although the reconstructed pressure signal is equal to zero for all the simulation time but the four events shown in Figs. 17, 18(a), 19(a), and 20(a), the filtered pressure has a rms value equal to 23.6% of the value for the original pressure time series. Thus, although the analyzed events are rare in the dynamics of the mixing layer, they are responsible for a significant portion of the sound power radiated by the flow, and they seem to have been the most easily suppressed by the optimal control.

We can conjecture that an optimal control applied to the extended simulation would again tend to eliminate these noisy events. In order to get a sense of the acoustic benefit which might be obtained, we compare in Fig. 21 pressure spectra for the original time series with spectra computed after the subtraction of the bursts of Figs. 17, 18(a), 19(a), and 20(a). We see that the suppressed events correspond to energy in a frequency band around $f=0.16f_0$. As shown by Wei and Freund, this corresponds to the loud peak in the acoustic field that is reduced by the optimal control.

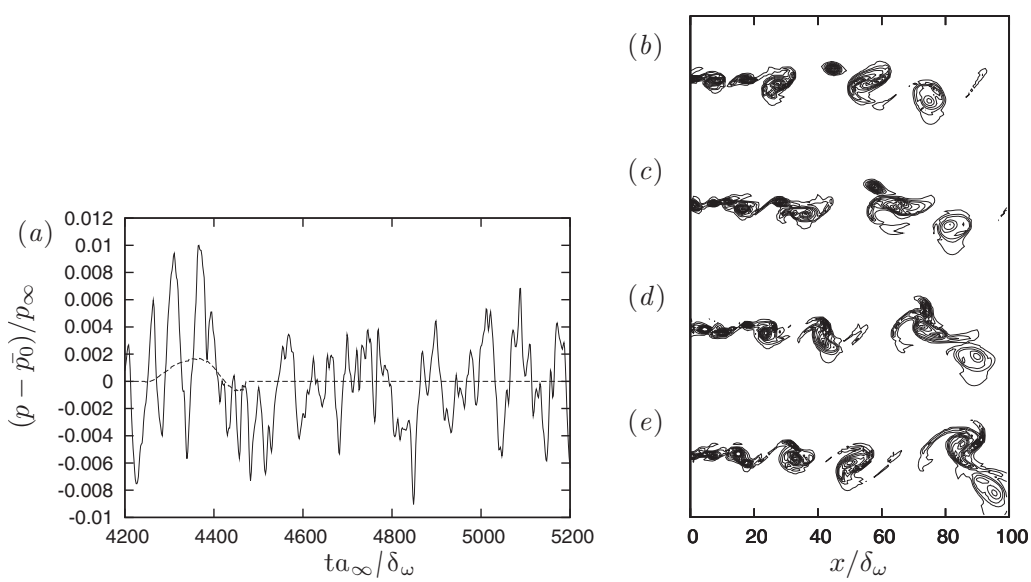

FIG. 19. (a) Wavelet filtering, (——) original and (- - -) filtered pressures. [(b)–(e)] Vorticity contours at ta_∞/δ_ω=4275.6, ta_∞/δ_ω=4292.4, ta_∞/δ_ω=4309.2, and ta_∞/δ_ω=4326.0. Same contours as Fig. 18.

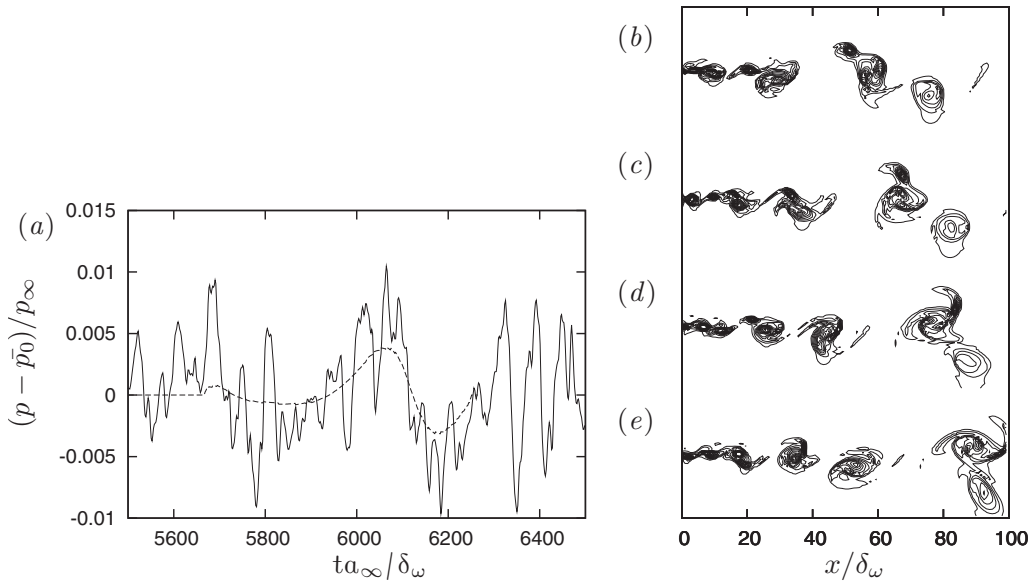

FIG. 20. (a) Wavelet filtering, (——) original and (- - -) filtered pressures. [(b)–(e)] Vorticity contours at ta_∞/δ_ω=5980.8, ta_∞/δ_ω=5997.6, ta_∞/δ_ω=6014.4, and ta_∞/δ_ω=6031.2. Same contours as Fig. 18.

V. CONCLUSION

An analysis was carried out to identify and understand the differences between the uncontrolled and controlled mixing layers of Wei and Freund.[4] The analysis of the pressure in the acoustic field showed that the noise reductions are especially significant in the downstream points of the target line, and 70% of the sound reduction in this region is achieved by the suppression of a high-amplitude pressure wave, comprising a compression followed by an expansion. A triple vortex interaction, which occurs only once in the simulation, is shown to lead to these peaks in sound pressure. Control was seen to comprise transverse vortex displacements, which, together with the consequent changes in convection velocity, modify the mutual interactions between neighboring structures in a way that prevents the triple vortex merger in the controlled mixing layer.

Wavelet transform analysis of a longer DNS calculation confirmed that loud events were associated with triple vortex mergers. These are intermittent events in the vortex dynamics of the mixing layer, but their contribution to the overall sound is considerable.

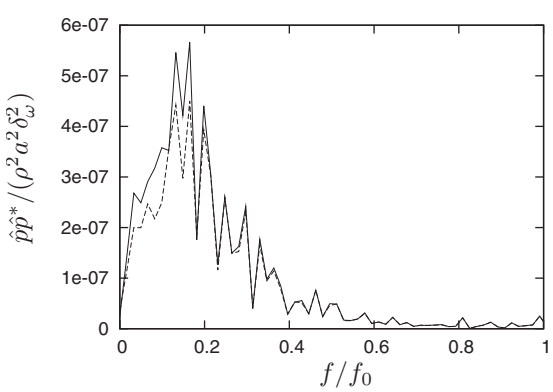

FIG. 21. Pressure spectra at $(80\delta_\omega, -70\delta_\omega)$: (——) original and (- - - -) suppression of bursts.

This study demonstrates (confirming the results of previous findings) that such intermittency constitutes a major element in the production of sound by free-shear flows. It should thus be explicitly included in modeling strategies. In many statistical noise prediction schemes such intermittent events are *not* explicitly included, and indeed they are often explicitly excluded by certain modeling assumptions. It is possible that this may explain the poor robustness of nearly all current sound prediction schemes. These are mostly based on second-order turbulence statistics, which, as we have seen, can entirely miss the most important sound producing events: the uncontrolled and controlled mixing layers present almost identical second-order statistics.

In interpreting our results, it should be clear that the plane mixing layer is a model flow that has been studied to determine the fundamental mechanisms of noise production.[15] However, the model problems of Cavalieri *et al.*,[13] with the incorporation of intermittency effects for the large scale structures of a free three-dimensional jet, have shown quantitatively how intermittent changes in a basic flow structure can generate bursts of noise in the far acoustic field of a turbulent jet. This intermittency does not need to be via a triple vortex merger as in the model flow studied in the present paper. Any significant disruption of the cancellation between the successive structures might lead to peaks in the acoustic field.

In terms of the details of the mechanism by which the propagative wave is set up, our study shows that this can be explained in terms of the kind of multipole interference that retarded-potential type solutions imply. This supports the idea that the acoustic analogy models are conceptually correct, though predictive modeling in a manner that incorporates intermittency effects is challenging. These points are the subject of ongoing modeling work.[13]

ACKNOWLEDGMENTS

The present work was supported by CNPq, National Council of Scientific and Technological Development-Brazil. J.B.F. and M.W. acknowledge support from AFOSR for the original mixing layer control simulations. J.B.F. acknowledges support from NASA for this work.

[1] M. J. Lighthill, "On sound generated aerodynamically. I. General theory," Proc. R. Soc. London, Ser. A **211**, 564 (1952).
[2] T. Colonius and S. K. Lele, "Computational aeroacoustics: Progress on nonlinear problems of sound generation," Prog. Aerosp. Sci. **40**, 345 (2004).
[3] M. Wang, J. B. Freund, and S. K. Lele, "Computational prediction of flow-generated sound," Annu. Rev. Fluid Mech. **38**, 483 (2006).
[4] M. Wei and J. B. Freund, "A noise-controlled free shear flow," J. Fluid Mech. **546**, 123 (2006).
[5] D. Eschricht, P. Jordan, M. Wei, J. B. Freund, and F. Thiele, "Analysis of noise-controlled shear-layers," in Proceedings of the 13th AIAA/CEAS Aeroacoustics Conference (28th AIAA Aeroacoustics Conference), American Institute of Aeronautics and Astronautics, 1801 Alexander Bell Drive, Suite 500, Reston, VA 20191-4344, 2007, Vol. 211, pp. 564–587.
[6] D. Juvé, M. Sunyach, and G. Comte-Bellot, "Intermittency of the noise emission in subsonic cold jets," J. Sound Vib. **71**, 319 (1980).
[7] J. I. Hileman, B. S. Thurow, E. J. Caraballo, and M. Samimy, "Large-scale structure evolution and sound emission in high-speed jets: Real-time visualization with simultaneous acoustic measurements," J. Fluid Mech. **544**, 277 (2005).
[8] J. Kastner, M. Samimy, J. Hileman, and J. B. Freund, "Comparison of noise mechanisms in high and low Reynolds number high-speed jets," AIAA J. **44**, 2251 (2006).
[9] J. B. Freund, "Noise sources in a low-Reynolds-number turbulent jet at Mach 0.9," J. Fluid Mech. **438**, 277 (2001).
[10] C. Bogey and C. Bailly, "An analysis of the correlations between the turbulent flow and the sound pressure fields of subsonic jets," J. Fluid Mech. **583**, 71 (2007).
[11] A. K. M. F. Hussain and K. B. M. Q. Zaman, "The 'preferred mode' of the axisymmetric jet," J. Fluid Mech. **110**, 39 (1981).
[12] J. E. Bridges and A. K. M. F. Hussain, "Roles of initial condition and vortex pairing in jet noise," J. Sound Vib. **117**, 289 (1987).
[13] A. V. G. Cavalieri, P. Jordan, A. Agarwal, and Y. Gervais, "Jittering wave-packet models for subsonic jet noise," Proceedings of the 16th AIAA/CEAS Aeroacoustic Conference and Exhibit, Stockholm, Sweden, 2010, AIAA Paper No. 2010-3957.
[14] A. V. G. Cavalieri, G. Daviller, P. Comte, P. Jordan, G. Tadmor, and Y. Gervais, "Using LES to explore sound-source mechanisms in jets," Procedia Engineering **6**, 104 (2010).
[15] T. Colonius, S. K. Lele, and P. Moin, "Sound generation in a mixing layer," J. Fluid Mech. **330**, 375 (1997).
[16] M. Wei, "Jet noise control by adjoint-based optimization," Ph.D. thesis, Department of Theoretical and Applied Mechanics, University of Illinois at Urbana-Champaign, Urbana, Illinois, 2004.
[17] M. Farge, "Wavelet transforms and their applications to turbulence," Annu. Rev. Fluid Mech. **24**, 395 (1992).
[18] C. Torrence and G. P. Compo, "A practical guide to wavelet analysis," Bull. Am. Meteorol. Soc. **79**, 61 (1998).